Chaos, Solitons and Fractals 161 (2022) 112318

Contents lists available at ScienceDirect

Chaos, Solitons and Fractals

Nonlinear Science, and Nonequilibrium and Complex Phenomena

journal homepage: www.elsevier.com/locate/chaos

Sensitivity of modeled tracer motion in tidal areas to numerics and to non-Hamiltonian perturbations

H.E. de Swart [a,*], S.T. van der Wal [a,b], J.E. Frank [b], G.P. Schramkowski [c]

[a] Utrecht University, Department of Physics, Institute for Marine & Atmospheric Research, P.O. Box 80005, 3508 TA Utrecht, the Netherlands
[b] Utrecht University, Mathematical Institute, Budapestlaan 6, 3584 CD, Utrecht, the Netherlands
[c] Flanders Hydraulics Research, Berchemlei 115, 2140 Antwerp, Belgium

ARTICLE INFO

Article history:
Received 22 January 2022
Received in revised form 14 May 2022
Accepted 7 June 2022
Available online xxxx

Keywords:
Lagrangian chaos
Tides
Splitting method
Orbit expansion

ABSTRACT

This study focuses on the motion of passive tracers induced by the joint action of tidal and residual currents in shallow seas with an irregular bottom topography. Interest in this problem has rapidly increased in recent years, because of the detection of large-scale pollution of marine waters by plastics. Early simplified models considered advection of tracers by a two-dimensional depth-averaged velocity field that is solenoidal, thereby resulting in a system that is Hamiltonian and nonintegrable. Here, two new aspects are considered. First, the sensitivity of solutions to three different numerical schemes is investigated. To quantify the behavior of orbits, both the largest Lyapunov exponent and the K-coefficient of the zero-one test for chaos were calculated. It turns out that a new scheme, which extends a known symplectic scheme to systems that also contain non-Hamiltonian terms, performs best. The second aspect concerns the fact that a depth-averaged velocity field is actually divergent, thereby rendering the model of tracer motion to be non-Hamiltonian. It is demonstrated that the divergent velocity components, no matter how small, cause the appearance of attractors in the system and thus they have a strong impact on the fate of tracers. Interpretation of the numerical results is given by deriving and analyzing approximate analytical solutions of the system.

1. Introduction

It has been demonstrated by Aref [1], Ottino [2] a.o. that, when tracers are released in unsteady two-dimensional (2D) and incompressible Eulerian velocity fields, the trajectories of some of these tracers are chaotic. The underlying process is called chaotic advection, or Lagrangian chaos. The reason for this behavior can be understood from the equations for 2D tracer motion $x(t)$, $y(t)$,

$$\dot{x} = u, \qquad \dot{y} = v, \tag{1}$$

with u and v the components of the Eulerian velocity field in the x- and y-direction, respectively. The dot denotes a total time derivative. Assuming the fluid to be incompressible, its velocity field has zero divergence, so in a 2D setting u and v are determined by a stream function ψ: $u = -\partial\psi/\partial y$ and $v = \partial\psi/\partial x$. When this is substituted in Eq. (1), it follows that the equations constitute a Hamilton system, with ψ representing the Hamiltonian. If ψ is time-dependent, the Hamilton system is nonintegrable and it will have a set of solutions that are chaotic (see e.g. Tabor [3]).

The concepts developed by [1] were subsequently used to study the behavior of passive tracers in tidal environments, such as the Wadden Sea, a shallow inland sea along the wadden coasts of the Netherlands, Germany and Denmark (Pasmanter [4], Ridderinkhof & Zimmerman [5], Beerens et al. [6]). The motivation for these studies was to gain more understanding about mixing processes in these areas, which is relevant for properly simulating the spreading and mixing of salt, sediment, nutrients, floating microplastics, etc. In these studies, a simple model was analyzed, in which the depth-averaged Eulerian velocity field consists of a spatially uniform tidal current and residual currents that are organized in alternating clockwise and anticlockwise horizontal circulation cells. The latter are due to the interaction of the tidal current with the bumpy bottom (Zimmerman [7]). The model has two control parameters, the first one being the ratio of tidal excursion length (the distance traveled by a parcel with maximum tidal current in one tidal period) and the spacing between successive residual cells. The second one is the ratio between the strength of the residual current and the maximum tidal current. These studies explicitly demonstrated the occurrence of local Lagrangian chaos and, for a range of parameter values, even global chaos, so that global mixing occurs. Moreover, [5],

* Corresponding author.
E-mail address: h.e.deswart@uu.nl (H.E. de Swart).

https://doi.org/10.1016/j.chaos.2022.112318

as well as later studies by e.g. Orre et al. [8] and Xu et al. [9], showed that Lagrangian chaos was also detected when tracers were advected by velocities obtained from numerical models of the Wadden Sea, a Norwegian fjord and Cobscook-Passamaquoddy Bay (Gulf of Maine, US), respectively.

Regarding the studies on tracer motion in tidal areas, several issues have received little attention so far. One of them concerns the numerical scheme used to solve the equations of motion (1). It is important that this scheme is chosen such that it maintains properties of the underlying differential equations. For example, the solutions shown in [6] were found with a numerical scheme (fourth-order Runge Kutta) that does not preserve the symplectic structure of the underlying Hamiltonian system and hence results in numerical inaccuracies that need to be quantified. Another issue is that Eulerian velocity fields obtained from depth-averaged models are two-dimensional, but yet they are divergent, because the depth of the fluid is not constant. Consequently, the tracer motion is not governed by a Hamiltonian system. In the analytical studies of [4,5] and [6] the divergent part of the velocity field was not taken into account, so their systems miss an essential aspect of tidal motion [8,9] accounted for the non-divergent component of the velocity field, but they did not systematically explore the effect of this component on the behavior of the tracers.

The previous considerations motivate the specific aims of this study, which are threefold. The first is to investigate the sensitivity of solutions of Eq. (1) to the applied numerical scheme. The second is to quantify the effect of the divergent part of the velocity field on tracer motion and the third is to explain the behavior of the system. To address the first aim, the model without non-Hamiltonian terms will be considered and solutions obtained by three different numerical methods will be compared. One of them is a new scheme that preserves the symplectic structure of the Hamiltonian part of the system. The comparison concerns the calculated largest Lyapunov exponent, using the method of Shimada & Nagashima [10] and Benettin et al. [11], as well the *K*-coefficient resulting from the '0–1 test for chaos' (Gottwald & Melbourne, [12,13]). The latter method does not quantify chaos, but it classifies an orbit as being chaotic or not.

The second aim will be met by analyzing output of numerical simulations of the full system, i.e., including the non-Hamiltonian terms. Insight into the system behavior (third aim) is achieved by studying approximate analytical solutions of the full system, which will be constructed by applying an orbit expansion [6]. Furthermore, a numerical bifurcation analysis will be performed on the periodic solutions of the system.

The contents of the subsequent sections is as follows. In Section 2 the model is presented, as well as three numerical schemes (ode45 of Matlab, Runge-Kutta 4 and a symplectic second-order scheme based on splitting) to solve the equations for the tracer orbits and brief information about the methods to characterize the behavior of these orbits. Section 3 outlines the orbit expansion method that results in approximate analytical solutions of the system. In Section 4 the results are presented, followed by a discussion (Section 5) and the final section contains the conclusions.

2. Material and methods

2.1. Model

The velocity field used in this study consists of the superposition of a background, spatially uniform tidal velocity field, characterized by a single radian frequency σ and amplitude U, and a topographically induced residual velocity field. The latter is obtained from solving the equations of motion for depth-averaged tidal currents over an irregular bottom topography, following [7,14] (see also Supplementary Information (SI) Appendix A). The depth is represented as an undisturbed, constant depth H, to which a perturbation h_* is added ($h_* > 0$ means larger depth). When assuming velocities to be scaled with U, time with σ^{-1}, depth with H and distances x and y with tidal excursion length U/σ, the equations of motion read

$$\dot{x} = u = \cos(t) - \frac{\partial \psi}{\partial y} + \frac{\partial \phi}{\partial x}, \tag{2a}$$

$$\dot{y} = v = \frac{\partial \psi}{\partial x} + \frac{\partial \phi}{\partial y}. \tag{2b}$$

In these expressions, ψ is the stream function and ϕ the velocity potential of the topographically induced velocity components. The velocity fields related to ψ and ϕ are solenoidal and irrotational, respectively.

The variables $x(t), y(t)$ indicate the position of any tracer S that obeys $dS/dt = 0$ in the Eulerian depth-averaged hydrodynamic model.[1] The model yields ψ and ϕ in terms of Fourier series, i.e.

$$(\psi, \phi) = \sum_{m=-\infty}^{\infty} \left(\psi_p, \phi_p\right) \exp(imt). \tag{3}$$

Topographic undulations are assumed to be small, i.e., $\hat{h} \ll H$, with $\hat{h}$ the scale of the bottom undulations. Furthermore, following [4–6], the dimensionless depth variations are represented as

$$h = \gamma \cos(\kappa x) \cos(\kappa y), \qquad \gamma = \frac{\hat{h}}{H}. \tag{4}$$

Here, κ is the topographic wavenumber scaled with the reciprocal of the excursion length U/σ. As $\gamma = \hat{h}/H$ is assumed to be small, approximate solutions for the velocity potential and stream function read

$$\phi = -\frac{1}{2}\frac{\gamma}{\kappa} \sin(\kappa x) \cos(\kappa y) \cos(t), \tag{5a}$$

$$\psi = -\frac{\nu}{\kappa} \sin(\kappa x) \sin(\kappa y). \tag{5b}$$

Thus, the velocity potential has the same time dependence as the background tidal current and only the residual part of the stream function is considered. The latter describes residual circulation cells that are generated by tide-topography interaction. Parameter ν is considered as an input parameter and its value measures the relative strength of the residual currents with respect to the maximum tidal current. A color plot of the dimensionless depth perturbation (blue is deep, red is shallow) and the dimensional residual stream function (scaled by its maximum value) is shown in Fig. 1. Substitution of these results in Eqs. (2a)–(2b) yields the model equations that will be investigated:

$$\dot{x} = \cos(t) + \nu \sin(\kappa x) \cos(\kappa y) - \frac{1}{2}\gamma \cos(\kappa x) \cos(\kappa y) \cos(t), \tag{6a}$$

$$\dot{y} = -\nu \cos(\kappa x) \sin(\kappa y) - \frac{1}{2}\gamma \sin(\kappa x) \sin(\kappa y) \cos(t). \tag{6b}$$

Earlier studies ([6] and references therein) ignored the contributions due to the velocity potential ($\gamma = 0$). In that case, the equations constitute a Hamilton system. Furthermore, in those studies a different scaling was used, in particular, horizontal coordinates were scaled with the topographic wavenumber and time was scaled with the tidal period instead of with the inverse radian frequency. The connection between the present formulation and that used in earlier studies is detailed in SI-Appendix B.

[1] When $ds/dt = 0$ is combined with mass conservation, it moreover follows that $d(SD\delta A)/dt = 0$, i.e., the amount of tracer in an infinitesimal fluid column of depth D and with surface area δA is conserved.

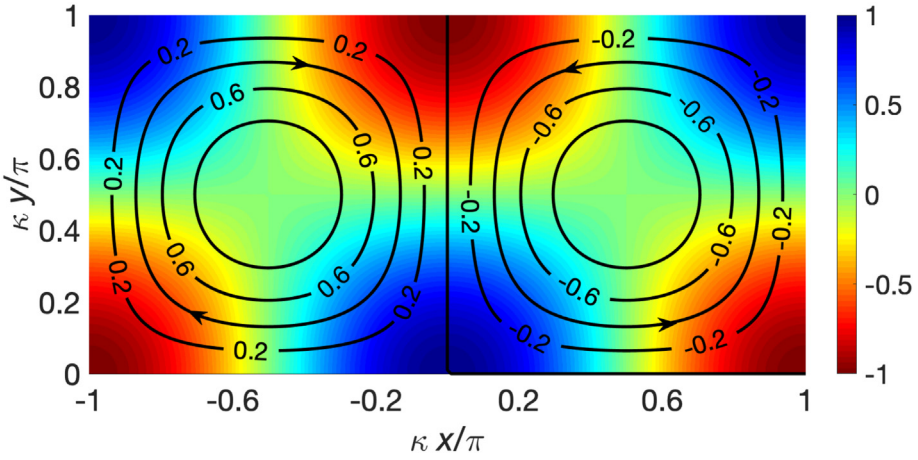

Fig. 1. Color plot of the dimensionless depth perturbation h, overlaid with contour plot of the residual stream function ψ (scaled by its maximum value). Blue colors denote positive h, i.e., larger than average depths, whilst red colors indicate negative h (smaller than average depth). Arrows indicate the direction of the residual currents. (For interpretation of the references to color in this figure legend, the reader is referred to the web version of this article.)

2.2. Numerical methods

Three different numerical schemes have been used to solve system (2a)–(2b). The first one is 'ode45', the default integrator of Matlab for systems of ordinary differential equations. The second scheme is the Runge-Kutta 4 scheme (hereafter RK4), a widely used explicit scheme that is of fourth order in the time step Δt (for details see e.g. Press et al. [15]). A disadvantage of both schemes is that, when they are applied to Hamiltonian systems, they do not preserve the symplectic structure (i.e., conservation of volume in phase space). A third scheme, based on a so-called symplectic splitting method (McLachlan & Quispel [16]), does not have that problem and it will be described in some more detail.

The idea behind splitting is that, given a vector field f of a dynamical system $\dot{z} = f(z,t)$ written as a sum of component vector fields whose flows are explicitly known, a consistent numerical integrator can be constructed as the composition of those solutions. For the present non-autonomous equations (6a) and (6b), a second-order scheme based on splitting is constructed by first applying the transformations

$$q = \kappa(x+y), \qquad p = \kappa(x-y). \tag{7}$$

Here, $q =$ constant and $p =$ constant are the phase lines of the two spatial Fourier modes that constitute the velocity potential ϕ and stream function ψ. Besides, an additional equation $\dot{t} = s$ is introduced. This results in

$$\dot{q} = \frac{\partial \mathcal{H}}{\partial p} + \frac{\partial V}{\partial q}, \quad \dot{p} = -\frac{\partial \mathcal{H}}{\partial q} + \frac{\partial V}{\partial p}, \qquad \dot{t} = \frac{\partial \mathcal{H}}{\partial s}, \quad \dot{s} = -\frac{\partial \mathcal{H}}{\partial t}, \tag{8}$$

where

$$\mathcal{H} = -\kappa \cos(t)(q-p) + 2\kappa^2 \psi(x(p,q), y(p,q)) + s, \tag{9a}$$

$$V = 2\kappa^2 \phi(x(p,q), y(p,q)) \tag{9b}$$

are the new Hamiltonian and the new potential. It turns out that $\mathcal{H}$ and V can be written as follows:

$$\mathcal{H} = s + \sum_{i=1}^{2} [F_i(q) + G_i(p)]\chi_i(t), \qquad V = [F(q) + G(p)]\chi(t), \tag{10}$$

where

$$F = -\frac{1}{2}\gamma \sin(q), \quad G = -\frac{1}{2}\gamma \sin(p), \quad \chi = \cos(t), \tag{11a}$$

$$F_1 = -\kappa q, \quad G_1 = \kappa p, \quad \chi_1 = \cos(t), \tag{11b}$$

$$F_2 = \kappa\nu \cos(q), \quad G_2 = -\kappa\nu \cos(p), \quad \chi_2 = 1. \tag{11c}$$

To ensure our method is symplectic for the case $\gamma = 0$, we use a Hamiltonian splitting. In our implementation we split $\mathcal{H} = \mathcal{H}_1 + \mathcal{H}_2$, with

$$\mathcal{H}_1 = s + \chi_1(t)(F_1(q) + G_1(p)), \qquad \mathcal{H}_2 = \chi_2(t)(F_2(q) + G_2(p)). \tag{12}$$

The $\mathcal{H}_1$ term leads to the dynamics

$$\dot{q} = \chi_1(t) G_1'(p), \quad \dot{p} = -\chi_1(t) F_1'(q), \tag{13a}$$

$$\dot{t} = 1, \quad \dot{s} = -\chi_1'(t)(F_1(q) + G_1(p)). \tag{13b}$$

Here, the prime indicates a derivative and we ignore the irrelevant conjugate variable s. We introduce a time transformation $d\tau = \chi_1(t)dt$ to reduce the system to

$$\frac{dq}{d\tau} = G_1'(p), \qquad \frac{dp}{d\tau} = -F_1'(q), \tag{14}$$

which is autonomous with respect to the new time variable. To construct a symplectic map for this system we split its (now autonomous) Hamiltonian to obtain either the map

$$q^{(i+1)} = q^{(i)} + \Delta\tau G_1\left(p^{(i)}\right), \qquad p^{(i+1)} = p^{(i)} - \Delta\tau F_1'\left(q^{(i+1)}\right), \tag{15a}$$

or its adjoint map

$$p^{(i+1)} = p^{(i)} - \Delta\tau F_1'\left(q^{(i)}\right), \qquad q^{(i+1)} = q^{(i)} + \Delta\tau G_1\left(p^{(i+1)}\right). \tag{15b}$$

The $\mathcal{H}_2$ term lends itself to a similar treatment, but since the s variable is excluded we find $\dot{t} = 0$. Furthermore, since $\chi_2 = 1$, no time transformation is required.

The full system is numerically solved by a scheme that is of second order, constructed by composing all split flows and their adjoints in a symmetric manner, analogous to the Störmer-Verlet method (Hairer et al. [17]). This results in the scheme as shown in Fig. 2. The potential terms are solved by applying the (time-symmetric) implicit midpoint rule for integrals [15] (here implemented as a half step of the backward Euler method followed by extrapolation). For the case $\gamma = 0$ this method has the important advantage of preserving the symplectic structure of the Hamiltonian dynamics.

The values of the numerical parameters in the three schemes (tolerances, time steps) were set as follows. First, note that system (6) has no analytical solutions or constants of motion that can be used to quantify the accuracy of the schemes. Therefore, a test system was considered, which bears some similarity with the present system (i.e., it also has a time-harmonic Hamiltonian) and which has non-trivial, yet analytical solutions. This test system reads

$$\dot{q} = p, \qquad \dot{p} = -(\alpha - \beta\cos(t))q, \tag{16}$$

which has solutions in terms of Mathieu functions (see SI-Appendix C). Several values for the parameters α and β and initial conditions $q(t = 0)$, $p(t = 0)$ were chosen for which solutions were quasi-periodic. Next, numerical solutions obtained with the three schemes were compared with exact solutions (retrieved with the software package Mathematica) and it was required that the relative error should be slightly less than 1% after 1000 forcing periods. For the ode45-scheme this implied that the absolute and relative tolerance had to be explicitly set, at values of $6 \cdot 10^{-6}$. Regarding RK4 and our scheme, the condition required 350, respectively 1000 time steps per forcing period. These values were subsequently used to find numerical solutions of system (6).

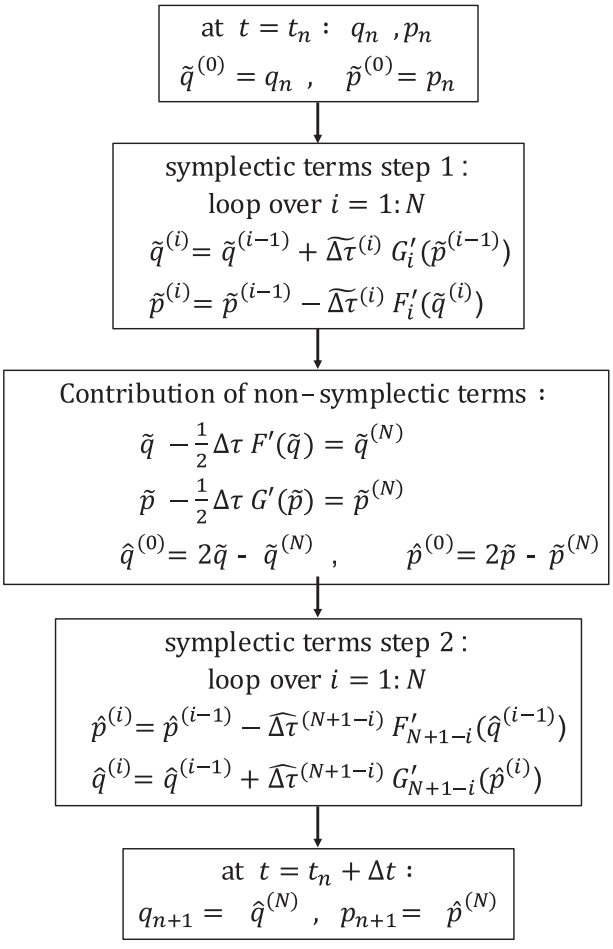

Fig. 2. Flow diagram of the numerical scheme that solves Eqs. (8)-(9) from time t_n to time $t_n + \Delta t$ and that preserves the symplectic structure of the Hamiltonian terms. In the present model, parameter $N = 2$, meaning that the Hamiltonian is split into two contributions. Furthermore, Δt is the time step, $\tilde{\Delta\tau}^{i} = \int_{t_n}^{t_n+\frac{1}{2}\Delta t} \chi_i(t)dt$, $\widehat{\Delta\tau}^{i} = \int_{t_n+\frac{1}{2}\Delta t}^{t_n+\Delta t} \chi_i(t)dt$ and $\Delta\tau = \int_{t_n}^{t_n+\Delta t} \chi_i(t)dt$.

2.3. Analysis of model output

2.3.1. Tidal maps

Model output is first used to construct tidal maps, which are a special kind of Poincaré maps: they show variables $x_j = x(t = t_j), y_j = y(t = t_j)$ at times $t_j = 2\pi j$, where $j = 0,1,2, \ldots$ and 2π is the dimensionless tidal period. Thus, tidal maps show the net displacement of tracers during a tidal period. If tides would be absent, the maps would reveal the stream lines of the residual current. In this study, tidal currents are assumed to be much larger than residual currents, so deviations from these stream lines are to be expected.

2.3.2. Largest Lyapunov exponent

Lyapunov exponents yield information about the time-mean exponential divergence rate of the distance between nearby orbits in phase space (see e.g. [3]). If at least one of these exponents is positive, the dynamics is chaotic. In the present 2D-time-dependent system, there are two non-trivial exponents and one additional exponent that relates to the explicit time behavior (its value being zero). Moreover, in the case that the system is Hamiltonian, Liouville's theorem implies that the sum of these exponents is zero.

In this study, we use the value of the largest Lyapunov exponent, called λ, to characterize the degree of chaos in the system. This exponent can be different for different tracer orbits. To calculate λ, a method developed separately by [10,11] was used. For this, the system (2a)–(2b) is solved, yielding a principal orbit $\bar{x}(t) = (\bar{x}(t), \bar{y}(t))$, together with its linearized tangent equations

$$\begin{aligned} \dot{x}' &= \left.\frac{\partial u}{\partial x}\right|_{\substack{x=\bar{x}\\ y=\bar{y}}} x' + \left.\frac{\partial u}{\partial y}\right|_{\substack{x=\bar{x}\\ y=\bar{y}}} y', \\ \dot{y}' &= \left.\frac{\partial v}{\partial x}\right|_{\substack{x=\bar{x}\\ y=\bar{y}}} x' + \left.\frac{\partial v}{\partial y}\right|_{\substack{x=\bar{x}\\ y=\bar{y}}} y'. \end{aligned} \tag{17}$$

The latter system describes the linear dynamics of small deviations from the principal orbit (indicated by primes). Next, define the following sequence:

$$\begin{aligned} x'_j(t) &= x'(2\pi(j-1) \le t \le 2\pi j), \\ y'_j(t) &= y'(2\pi(j-1) \le t \le 2\pi j), \end{aligned} \tag{18}$$

where x', y' are solutions of the tangent map, with initial conditions

$$x'_1(0) = \cos(\varphi), \qquad y_1(0) = \sin(\varphi), \tag{19a}$$

$$x'_{j+1}(2\pi j) = x'_j(2\pi j)/d_j, \qquad y'_{j+1}(2\pi j) = y'_j(2\pi j)/d_j. \tag{19b}$$

In these expressions, φ may be assigned any value and

$$d_j = \left(x'_j(2\pi j)^2 + y'_j(2\pi j)^2\right)^{1/2} \tag{20}$$

is a distance.

The procedure is that at $t = 0$ an initial condition for x', y' is imposed with norm $= 1$, so the initial distance $d_0 = 1$. Next, the system is integrated over one tidal period and the distance d_1 is calculated. Subsequently, the solution is normalized with d_1, so that the solution

for the next tidal period has again an initial condition that has a distance equal to 1. This step is made to prevent overflow (the solutions of the tangent map may grow exponentially in time) and it can be done because the tangent map is linear. After that, the integration over the next tidal period is performed, which yields d_2, etc. A numerical estimate of the largest Lyapunov exponent is computed as

$$\lambda \simeq \lambda_J = \frac{1}{2\pi J}\sum_{j=1}^{J} \ln\,(d_j), \tag{21}$$

with J the total number of tidal cycles used to calculate the coefficient. Its value is such that $|\lambda_J - \lambda_{J-1}| \le \max\,(\epsilon_a, \epsilon_r \lambda_{J-1})$, where ϵ_a and ϵ_r are a user-specified absolute tolerance and relative tolerance, respectively.

2.3.3. 0–1 test for chaos

In practice, accurate calculation of the largest Lyapunov exponent is difficult in the case of weak chaos. To obtain additional support for whether a small positive exponent indicates chaos, or if the interest is more on knowing whether an orbit is chaotic or not, the '0–1 test for chaos' developed by [12] (see also the review by [13]) is a suitable alternative.

The numerical implementation of this method consists of four steps. First, from a given time series $\phi(j), j = 1, 2, \ldots, N$, in the present model $\phi(j) = y(t = 2\pi j)$ is chosen, the following so-called translation variables are defined:

$$\begin{aligned} p_c(N) &= \sum_{j=1}^{N} \phi(j)\,\cos\,(jc), \\ q_c(N) &= \sum_{j=1}^{N} \phi(j)\,\sin\,(jc), \end{aligned} \tag{22}$$

for any $c \in (0,\pi)$.

Next, the mean-square displacement

$$M_c(n,N) = \frac{1}{N-n}\sum_{j=1}^{N-n}\left\{[p_c(j+n) - p_c(j)]^2 + [q_c(j+n) - q_c(j)]^2\right\} \tag{23}$$

is analyzed for $N \gg n \gg 1$. For a chaotic signal $M_c(n \gg 1)$ grows linearly with n, whilst for non-chaotic signals $M_c(n \gg 1)$ approaches a constant. Based on this, the following mean asymptotic growth rate is calculated:

$$\begin{aligned} K &= \text{median}(K_c), \\ K_c &= \frac{\ln\,(M_c(n,,N))}{\ln\,(n)} \quad \text{for } N \gg n \gg 1. \end{aligned} \tag{24}$$

The test is expected to yield a value $K = 0$ (regular dynamics) or $K = 1$ (chaotic dynamics. If this is not the case, then typically a larger N is needed. The reason to calculate the asymptotic growth rates for different values of c is that for some isolated values of c the method yields outliers of K_c. Further details are given in [13] and references therein.

2.4. Design of numerical experiments

A list of experiments is presented in Table 1. In order to meet the first specific aim of this study, system (6) with $\gamma = 0$ was considered, so the equations governing the tracer motion constitute a Hamiltonian system. Solutions for parameter values $\nu = 0.3$ and $\kappa = \pi/2, \pi$ were computed using three different numerical schemes: ode45, RK4 and the one that is based on the splitting method and preserves the (in this configuration) symplectic structure of the system. The reason to choose the first two parameter values is that they reveal interesting behavior [6]. Results for other parameter values are presented in SI-Appendix E.

In all experiments, the absolute and relative tolerance for calculating the Lyapunov exponents were set to $\epsilon_{abs} = 1 \cdot 10^{-4}$ and $\epsilon_{rel} = 0.002$. For the 0–1 test, following recommendations by [13], a total of 5000 data points were used, a fraction of 10% was used to calculate the mean-square displacements $M_c(n,N)$ in Eq. (23) and a total number of 100 values for parameter c was used, which were uniformly distributed over the interval $(\pi/5, 4\pi/5)$.

The experiments of Series 2 were designed to meet the second aim, i.e., to quantify the effects of including the non-Hamiltonian terms in model (6), hence $\gamma > 0$.

3. Construction of approximate solutions and related tidal map

To interpret the model behavior, approximate analytical solutions of system (6), as well as an approximate tidal map, were derived by applying the method of orbit expansion [6]. This method assumes that parameters $\nu \ll 1$, $\gamma \ll 1$, so the background tidal current is the dominant agent for tracer motion. The new aspects in this section are that solutions are derived and analyzed for the system up to $\mathcal{O}(\nu^2, \nu\gamma)$.

Instead of using Eqs. (6a) and (6b), it is more convenient to transform x, y to the new canonical variables p, q, which were defined in Eq. (7). This results in

$$\dot{q} = \kappa\,\cos\,(t) + \widehat{\nu}\,\sin\,(p) - \widehat{\gamma}\,\cos\,(t)\,\cos\,(q), \tag{25a}$$

$$\dot{p} = \kappa\,\cos\,(t) + \widehat{\nu}\,\sin\,(q) - \widehat{\gamma}\,\cos\,(t)\,\cos\,(p), \tag{25b}$$

in which

$$\hat{\nu} = \kappa\nu, \qquad \hat{\gamma} = \frac{1}{2}\kappa\gamma \tag{26}$$

and with initial conditions $q(t=0) = q_*$, $p(t=0) = p_*$. The advantage of this system is its cyclic structure: the equation for the evolution of p directly follows from that for q by exchanging q and p.

Application of the orbit expansion yields

$$q = q_0 + q_1 + q_2 \ldots, \qquad p = p_0 + p_1 + p_2 \ldots, \tag{27}$$

where

$$\dot{q}_0 = \cos(t), \qquad \dot{p}_0 = \cos(t), \tag{28a}$$

$$\dot{q}_1 = \dot{q}\Big|_{\substack{q=q_0\\p=p_0}} - \dot{q}_0, \qquad \dot{p}_1 = \dot{p}\Big|_{\substack{q=q_0\\p=p_0}} - \dot{p}_0, \tag{28b}$$

$$\dot{q}_2 = \dot{q}\Big|_{\substack{q=q_0+q_1\\p=p_0+p_1}} - \dot{q}_0 - \dot{q}_1, \quad \dot{p}_2 = \dot{p}\Big|_{\substack{q=q_0+q_1\\p=p_0+p_1}} - \dot{p}_0 - \dot{p}_1, \tag{28c}$$

etc. The zeroth-order system, which only includes advection of tracers by the background tidal current, can be straightforwardly solved:

$$q_0 = q_* + \kappa\,\sin\,(t), \quad p_0 = p_* + \kappa\,\sin\,(t). \tag{29}$$

Substitution of these results into the first-order equations (28b) yields

$$\dot{q}_1 = \hat{\nu}\,\sin(p_* + \kappa\,\sin(t)) - \hat{\gamma}\,\cos(t)\,\cos(q_* + \kappa\,\sin(t)) \tag{30}$$

and a similar equation for $\dot{p}$, which directly follows from the cyclic structure of the system. From hereon, only solutions for q will be explicitly written. The solution of the above equation reads

Table 1
List of experiments. Experiment Series 1 tests three different numerical methods: symplectic, ode45 (Matlab) and RK4. In all other experiments, the explicit scheme based on the splitting method (Section 2.2) was used.

Experiment Series	ν	κ	γ
1: Numerics-Hamiltonian	0.3	$\pi/2, \pi$	0
2: Non-Hamiltonian	0.1-0.3	1-10	0.3-0.6

$$q_1 = \hat{\nu}[\ \sin(p_*)\, F_c(t) + \ \cos(p_*)\, F_s(t] + \hat{\gamma}[-\ \cos(q_*)\, F_{cc}(t) + \ \sin(q_*)\, F_{cs}(t)], \tag{31}$$

in which

$$F_c(t) = \int_0^t \cos\,(\kappa\,\sin\,(t'))\,dt', \qquad F_s(t) = \int_0^t \sin\,(\kappa\,\sin\,(t'))\,dt', \tag{32a}$$

$$F_{cc}(t) = \int_0^t \cos\,(t')\,\cos\,(\kappa\,\sin\,(t'))\,dt' = \frac{1}{\kappa}\,\sin\,(\kappa\,\sin\,(t)), \tag{32b}$$

$$F_{cs}(t) = \int_0^t \cos\,(t')\,\sin\,(\kappa\,\sin\,(t'))\,dt' = \frac{1}{\kappa}[1 - \ \cos\,(\kappa\,\sin\,(t))]. \tag{32c}$$

Next, we consider the second-order system (28c). As $\hat{\nu} \ll 1, \hat{\gamma} \ll 1$, the magnitude of q_1 is much smaller than that of q_0. Maintaining only the dominant contributions yields

$$\dot{q}_2 = \hat{\nu}\,\cos(p_0)\,p_1 + \hat{\gamma}\,\cos(t)\,\sin(q_0)\,q_1. \tag{33}$$

Upon substitution of the zeroth-order and first-order solutions (28a)–(28b), the solution for q_2 (and for p_2) is obtained (for the full expression see SI-Appendix D).

The preceding information is used to construct a second-order tidal map, by expressing $q(t = 2\pi), p(t = 2\pi)$ in terms q_*, p_*, i.e., the values of q, p one period earlier. From Eqs. (28a), (28b), it follows

$$q_0(2\pi) = q_*, \qquad q_1(2\pi) = 2\pi\hat{\nu}J_0(\kappa)\,\sin\,(p_*) \tag{34}$$

and similar expressions for $p_0(2\pi), p_1(2\pi)$. In the derivation of $q_1(2\pi), p_1(2\pi)$ the identity [18].

$$\int_0^{2\pi} \exp\,(\mathrm{i}\kappa\,\sin\,(t'))dt' = 2\pi J_0(\kappa) \tag{35}$$

has been used, with i the imaginary number and $J_0(\kappa)$ the zeroth-order Bessel function. To evaluate $q(2\pi)$, results (C1.1) and (C4a) of SI-Appendix D are used. Finally writing

$$q_j = q_*, \qquad q_{j+1} = q_0(2\pi) + q_1(2\pi) + q_2(2\pi), \tag{36a}$$

$$p_j = p_*, \qquad p_{j+1} = p_0(2\pi) + p_1(2\pi) + p_2(2\pi), \tag{36b}$$

where subscripts from hereon refer to the iteration number of the map, it follows

$$q_{j+1} = q_j + 2\pi\hat{\nu}J_0(\kappa)\,\sin\left(p_j\right) + \pi^2\hat{\nu}^2J_0(\kappa)\Big[2J_0(\kappa)\,\sin\left(q_j\right)\cos\left(p_j\right) + \mathbf{H}_0(\kappa)\,\cos\left(q_j - p_j\right)\Big] + \hat{\nu}\hat{\gamma}\frac{\pi}{\kappa}\Big\{-\ \sin\left(q_j - p_j\right) - 2J_0(\kappa)\Big[\cos\left(q_j\right) - \ \cos\left(p_j\right)\Big]\sin\left(p_j\right) + J_0(2\kappa)\Big[\sin\left(q_j + p_j\right) - \ \sin\left(2p_j\right)\Big]\Big\} \tag{37}$$

and a similar equation for p_{j+1}. In this result, $\mathbf{H}_0(\kappa)$ is the zeroth-order Struve function, which for convenience is plotted in Fig. 3 (for its appearance see SI-Appendix D).

Together, these equations constitute the tidal map in q, p-variables. Note that there are no contributions that are proportional to $\hat{\gamma}$ and $\hat{\gamma}^2$. These findings are subsequently transformed back to x, y-variables, yielding

$$x_{j+1} = x_j + 2\pi\nu J_0(\kappa)\,\sin\,(\kappa x_j)\,\cos\left(\kappa y_j\right) + \pi^2\kappa\nu^2J_0(\kappa)\Big[J_0(\kappa)\,\sin\,(2\kappa x_j) + \mathbf{H}_0(\kappa)\,\cos\left(2\kappa y_j\right)\Big] + \frac{1}{2}\pi\nu\gamma\,\sin\,(2\kappa x_j)\Big[1 - \ \cos\left(2\kappa y_j\right)\Big], \tag{38a}$$

$$y_{j+1} = y_j - 2\pi\nu J_0(\kappa)\,\cos\,(\kappa x_j)\,\sin\left(\kappa y_j\right) + \pi^2\kappa\nu^2J_0^2(\kappa)\,\sin\left(2\kappa y_j\right) - \frac{1}{2}\pi\nu\gamma\Big[\sin\left(2\kappa y_j\right) + 4J_0(\kappa)\,\sin\,(\kappa x_j)\,\sin\left(\kappa y_j\right) - J_0(2\kappa)\,\cos\,(2\kappa x_j)\,\sin\left(2\kappa y_j\right)\Big]. \tag{38b}$$

The first-order map is identical to that presented in [6]. The $\mathcal{O}(\nu^2)$ terms are corrections on those in that paper, which resulted from a mistake in the derivation. The $\mathcal{O}(\nu\gamma)$-terms are new.

We now briefly discuss the fixed points of the tidal map (37), here denoted as $q_j = \hat{q}, p_j = \hat{p}$. They represent periodic solutions of the underlying differential equations. As $\hat{\nu} \ll 1, \hat{\gamma} \ll 1$, approximations of these fixed points can be constructed as

$$\hat{q} = Q_{00} + \hat{\nu}Q_{10} + \hat{\gamma}Q_{01} + \ldots, \qquad \hat{p} = P_{00} + \hat{\nu}P_{10} + \hat{\gamma}P_{01} + \ldots. \tag{39}$$

Substitution into the tidal map equations and analyzing the results at different orders yields

$$\sin\,(Q_{00}) = 0 \quad \text{so} \quad Q_{00} = m\pi \quad (m \in \mathrm{Z}), \tag{40a}$$

$$\sin\,(P_{00}) = 0 \quad \text{so} \quad P_{00} = n\pi \quad (n \in \mathrm{Z}), \tag{40b}$$

$$Q_{10} = (-1)^{n+1}\,\frac{\pi}{2}\,\mathbf{H}_0(\kappa), \qquad Q_{01} = 0, \tag{40c}$$

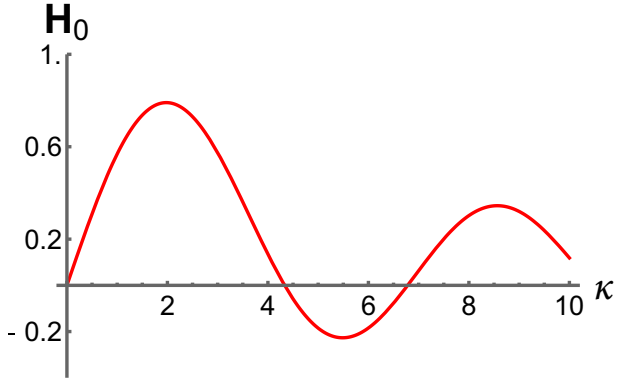

Fig. 3. Plot of the zeroth-order Struve function $\mathbf{H}_0(\kappa)$, which appears in the second-order tidal maps (37), (38a) and (38b).

$$P_{10} = (-1)^{m+1}\frac{\pi}{2}\mathbf{H}_0(\kappa), \qquad P_{01} = 0. \tag{40d}$$

These results imply that, when $\widehat{\nu}, \widehat{\gamma} \ll 1$, fixed points occur in the vicinity of $q = m\pi$, $p = n\pi$. The latter are the corner points of the residual circulation cells when $(m + n)$ is even and the midpoints of the cells when $(m + n)$ is odd. The effect of increasing $\widehat{\nu}$ is that their locations shift: those near the corner points shift only in the x-direction, whereas those near the midpoints shift only in the y-direction. The direction of the shifts is controlled by $\mathbf{H}_0(\kappa)$. For example, when κ is smaller than the first zero of $\mathbf{H}_0(\kappa)$, which occurs at $\kappa \simeq 4.33$, fixed points are to the left of the bottom-left and top-right corner, to the right of the top-left and bottom-right corner and below the center point. Interestingly, variations in $\widehat{\gamma}$ do not affect these fixed points, so periodic solutions for $\widehat{\gamma} = 0$ are also periodic solutions for small $\widehat{\gamma}$.

Finally, we consider the stability of the fixed points of the map for $\widehat{\gamma} = 0$. In that case, the map is (to $\mathcal{O}(\nu^3)$) symplectic and thus the stability of fixed points is determined by the trace Tr of the tangent map, i.e. $Tr = \partial q_{j+1}/\partial q_j + \partial p_{j+1}/\partial p_j$, evaluated at the fixed points (see e.g. Section 4.3 in [3]). It turns out that $Tr > 2$ when $(m + n)$ is even, meaning that these fixed points (located close to the corner points) have two real eigenvalues, one smaller and one larger than 1. Consequently, they are unstable, hyperbolic points. When $(m + n)$ is odd, $Tr < 2$, so two complex eigenvalues (which are each other's conjugates) with modulus 1 are obtained. These fixed points, located near the midpoints of the cells, are center points and thus Lyapunov stable. The effect of setting $\widehat{\gamma} > 0$ will be presented and discussed in subsequent sections.

4. Results

4.1. Sensitivity of model results to numerical scheme

Fig. 4 shows tidal maps and time series, calculated with the symplectic code for model (6), assuming $\gamma = 0, \nu = 0.3$, and two different values of the dimensionless topographic wavenumber: $\kappa = \pi/2$ and $\kappa = \pi$. The time step was $\Delta t = 2\pi/1000$ (see Subsection 2.2). Different initial conditions were chosen in the domain $-\pi \le \kappa x \le \pi$, $0 \le \kappa y \le \pi$. As shown in Fig. 1, this domain covers two cells with clockwise and anticlockwise residual circulations in the left half and right half of the domain, respectively.

Note that it seems that the tidal maps are invariant under the transformation $(x, y) \to (-x, \frac{\pi}{\kappa} - y)$, but a closer inspection reveals that this is not the case. Instead, the equations are invariant under the transformations $(x, y, t) \to (x + 2n_x\pi/\kappa, y + 2n_y\pi/\kappa, t)$ and $(x, y, t) \to (-x, -y, t + (2n_t - 1)\pi)$, with n_x, n_y and n_t being integers. This explains why the domains shown cover at least two adjacent residual circulation cells.

Tidal maps, for the same parameter values and initial conditions as in Fig. 4, were also generated with two other numerical schemes: ode45 and RK4. The results (not shown) are overall similar, i.e., the same patterns are found. However, run times were different. For $\kappa = \pi/2$ the code with the symplectic scheme took approximately 8 s with Matlab -R019B on a Macbook Air. For ode45 and RK4 the run times were a factor ~2, respectively ~5, longer. Thus, besides preserving the symplectic structure of the Hamiltonian part of the system, the new code is also faster.

The tidal map for $\kappa = \pi/2$ (Fig. 4a) reveals the existence of both elliptical points (in the interior) and hyperbolic points (at the boundaries $y = 0$ and $y = \kappa\pi$). The presence of these fixed points was demonstrated in Section 3. There are many regular orbits, which loop around the elliptical points. The sense of revolution of these orbits is identical to that of the residual circulation cells, i.e., clockwise in the left part of the domain and anticlockwise in the right part. However, for initial conditions with $y(t = 0)$ close to $y = 0$ or $y = 1$, chaotic trajectories appear (see also the time series of $\kappa x/\pi$ $\kappa y/\pi$ and in panels b and c). These orbits remain close to stable and unstable manifolds of the hyperbolic points that are located at $y = 0$ and $y = 1$. When orbits get close to these hyperbolic points the orbits may cross the border of the domain and enter a different cell.

For $\kappa = \pi$ (Fig. 4d), the area with regular orbits is smaller than that in panel a and much more orbits are chaotic (some time series are shown in panels e and f). The regular orbits are also more complex than those in panel a: the closed blue curve and red curve each enclose an area where quasi-periodic solutions occur with a dominant period that is three times the period of the imposed tide. Moreover, in contrast to the previous case, regular solutions now revolve in a direction that is opposite to that of the residual circulation. The latter implies that the residual Lagrangian velocity (i.e., the net displacement of parcels in one tidal period) opposes the Eulerian velocity. This is due to Stokes drift [19], which results from the fact that a moving tracer experiences at each time a velocity that differs from the velocity at the initial point.

The difference in direction of revolution of regular orbits between $\kappa = \pi/2$ and $\kappa = \pi$ can be explained from the approximate analytical tidal map (38). This map shows that the sense of rotation changes at values $\kappa = \kappa_n$ that are zeros of Bessel function $J_0(\kappa)$, i.e. $\kappa_1 = 2.4048..$, $\kappa_2 = 5.5201..$, etc. [18]. According to (38), for these values all points in the domain are fixed points, implying the occurrence of global bifurcations. As is detailed in SI-Appendix E, the numerical tidal map shows similar, yet slightly different behavior. It turns out that in the vicinity of κ_n (for example, in the range $1.97 < \kappa < 2.58$), a series of ordinary bifurcations occur that ultimately result in the change in sense of revolution of orbits about elliptical points.

4.2. Quantification of chaos and dependence of results on the numerical scheme

Color plots of the computed largest Lyapunov exponent for different initial conditions in the domain are shown in Fig. 5 for the parameters $\nu = 0.3$ and $\kappa = \pi/2$. Similar plots are shown in Fig. 6 for $\nu = 0.3$ and $\kappa = \pi$. The different panels in each figure are for our numerical scheme (default setting, 1000 time steps per tidal cycle), the same scheme with 1500 time steps per tidal cycle, the ode45 scheme with abstol = reltol= $6 \cdot 10^{-6}$) and the RK4 scheme with 350 time steps per tidal cycle.

For $\kappa = \pi/2$, the largest Lyapunov exponent has a value of 0.03 (panel a), which means that small perturbations on the chaotic orbit grow a factor e in (1/0.03) tidal periods. Furthermore, for most initial conditions (those in the blue area in panel a) the resulting orbits are regular. Chaotic behavior may occur when initial conditions are chosen close to the stable and unstable manifolds of the hyperbolic points at $y = 0$ ($x \simeq -0.15\kappa\pi$ and $x \simeq -0.85\kappa\pi$) and at $y = \kappa\pi$ ($x \simeq 0.15\kappa\pi$ and $x \simeq 0.85\kappa\pi$). When the time step in the symplectic scheme is increased from 1000 to 1500 steps per tidal cycle, differences are very small for most initial conditions (panel b). There are however isolated initial conditions near the stable and unstable manifolds where one numerical setting yields a zero maximum exponent, whereas the other setting yields a positive value. These 'spikes' do not disappear when the time step is further reduced. Their occurrence is probably due to the fact that near these manifolds a complex pattern of both chaotic and regular orbits occurs. Which orbit is realized for a given initial condition near these manifolds depends on the time step and the outcome is erratic, no matter how small the time step. We will return to this aspect in Section 5.

When Lyapunov exponents are calculated with ode45, and with RK4, results are quite similar to those obtained for the default setting, except for isolated initial conditions. The main differences are that ode45 and RK4 are slower (by a factor of ~2 and ~5, respectively) than our symplectic code.

In case that the topographic wavenumber $\kappa = \pi$, the largest value of the Lyapunov exponent is about 0.07 and, compared to the previous case, much more initial conditions result in chaotic orbits

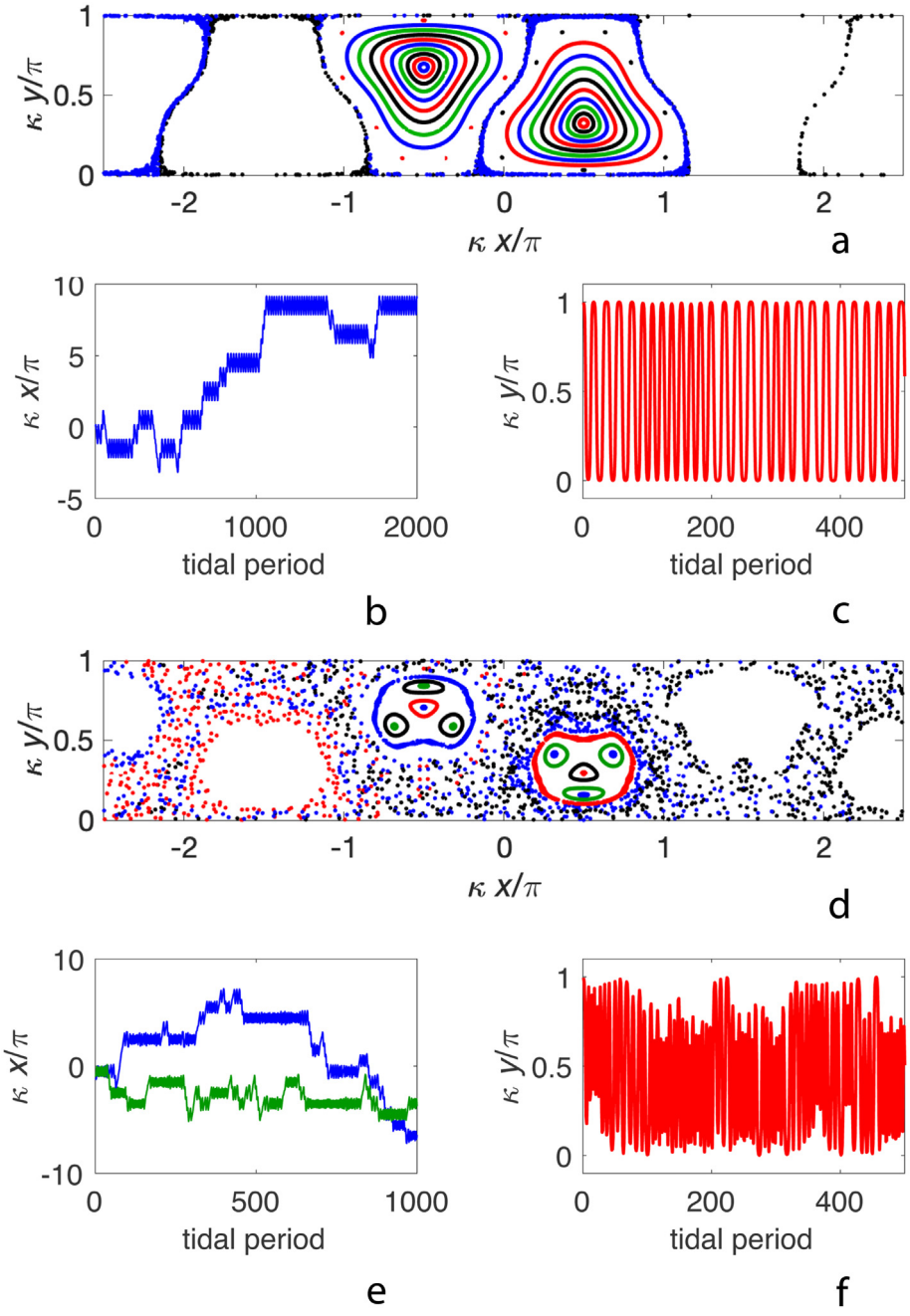

Fig. 4. a. Tidal map for $\gamma = 0$, $\nu = 0.3$, $\kappa = \pi/2$, symplectic method, 1000 time steps per tidal period, number of tidal periods $N = 2000$. Initial conditions for $\kappa = \pi/2$: $\kappa x/\pi = -0.5001$, $\kappa y/\pi = 0.999$ down to 0.7 with steps of 0.03 and $\kappa x/\pi = 0.5001$, $\kappa y/\pi = 0.001$ up to 0.3 with steps of 0.03. b. Time series of $\kappa x/\pi$ of the first orbit shown in panel a at multiples of the imposed tidal period. c. As panel b, but for $\kappa y/\pi$. d. As panel a, but for $\kappa = \pi$, $N = 1000$; initial conditions for $\kappa = \pi$: as in a., but steps of 0.05 and down to 0.7/up to 0.3. e. Time series of $\kappa x/\pi$ of the first two orbits shown in panel d at multiples of the imposed tidal period. f. As panel e, but for $\kappa y/\pi$ of the first orbit.

(Fig. 6a). Still, there are two relatively large (blue) areas where orbits will behave regular. Note that outside these areas, there are small sets of initial conditions for which orbits are regular. Likewise, inside these areas there are subsets of initial conditions (light-blue points) for which orbits will be weakly chaotic (largest Lyapunov exponent of about 0.01).

When decreasing the time step of the symplectic code, again different values of Lyapunov exponents are found for specific initial conditions (Fig. 6b). The latter are mainly found around the fringes of the blue areas shown in panel a. Similar isolated differences in values of the Lyapunov exponents are seen when the default scheme is compared with ode45 and RK4 (Fig. 6c,d). Regarding the computational time, also for this setting ode45 and RK4 perform much slower than the default scheme.

Fig. 7 shows the results of the zero-one test for chaos for the two cases that are considered in this subsection. There is a clear correlation between the values of the K-coefficient and those of the largest Lyapunov exponent (compare Fig. 7a with Fig. 5a and Fig. 7b with Fig. 6a). The calculated K-coefficients further confirm that for $\kappa = \pi$ there are two larger areas where mostly regular orbits occur, but inside these areas small bands of initial conditions are found that result in chaotic orbits. Conversely, in the large area where mostly chaotic orbits occur, there are small subareas of initial conditions for which orbits will behave regularly.

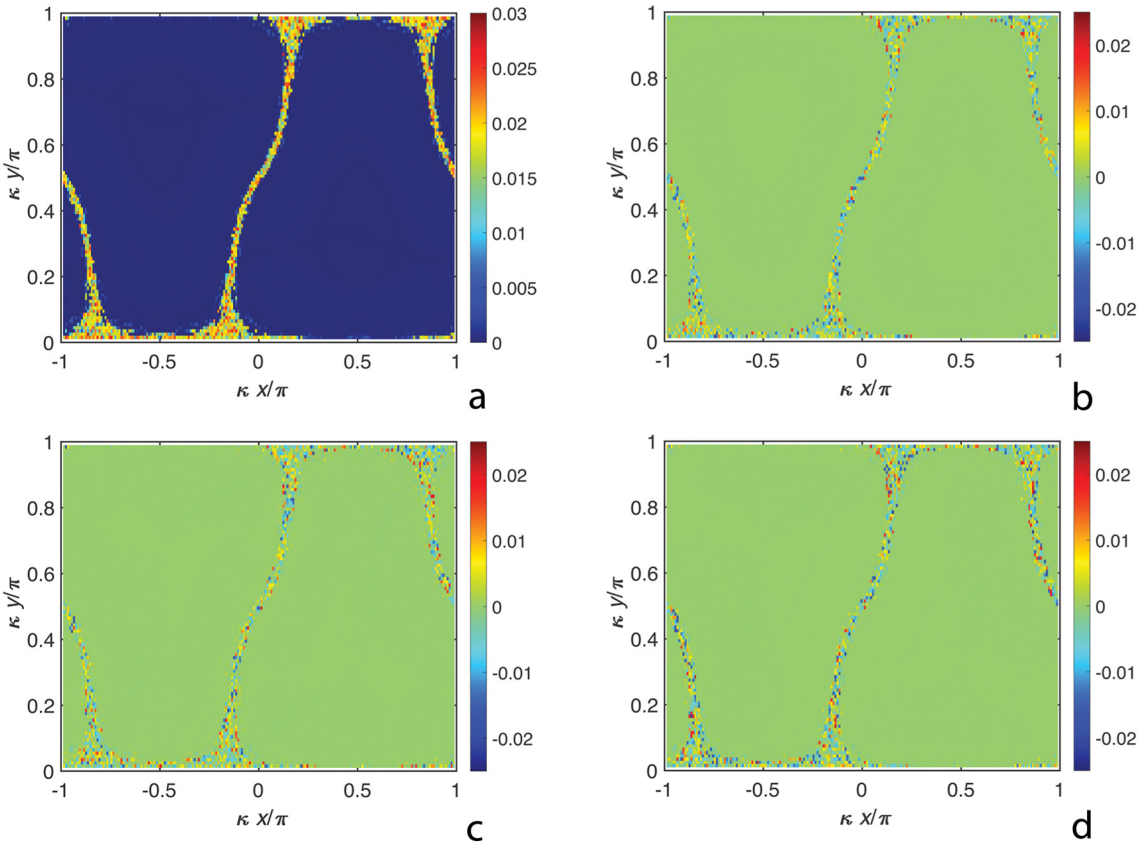

Fig. 5. a: Color plot of the largest Lyapunov exponent ($\kappa = \pi/2$, $\nu = 0.3$) as a function of initial conditions in the $x - y$-plane, default setting (symplectic method, 1000 steps/tidal cycle, absolute tolerance <0.0002, relative tolerance <0.01. b) Difference plot of the largest Lyapunov exponent calculated by the symplectic method, 1500 steps/tidal cycle, with respect to the default setting. c. As b, but for ode45 (abstol = reltol = $6 \cdot 10^{-6}$) with respect to default. d. As b., but for RK4-350 steps/tidal cycle with respect to default. (For interpretation of the references to color in this figure legend, the reader is referred to the web version of this article.)

4.3. Effects of non-Hamiltonian velocity field on tracers motion

Fig. 8 shows tidal maps for the same parameter values as in Fig. 4, but now the velocity field includes a contribution that originates from potential ϕ. The magnitude of the latter term is measured by parameter γ. Here, $\gamma = 0.01$, so a weakly perturbed Hamilton system is considered. The perturbed velocity field causes the system to have multiple attractors, which are either periodic or strange attractors. They are located in the areas where the Hamiltonian system has chaotic orbits (i.e., the red areas in Fig. 7). The transient motion towards these attractors is in the order of 100 tidal periods. Thus, tracer material moves to specific regions of the phase space, but their precise orbits strongly depend on the initial condition. The distribution of Lyapunov exponents in the $x - y$ phase space (not shown) is quite erratic, i.e., there are no large connected areas of initial conditions for which the nontransient motion will be periodic or chaotic.

Fig. 9 shows another example of how the potential terms destroy the Hamiltonian structure of the system. In this case $\nu = 0.04$ and two values of the topographic wavenumber are considered: $\kappa = \pi/2$ (left panels) and $\kappa = \pi$ (right panels). The upper panels show tidal maps for the Hamilton system, i.e. $\gamma = 0$. Fixed points (near the corners of the domain, as well as two near the centres of the residual circulation cells) and closed orbits are found. Thus, solutions $x(t)$, $y(t)$ of system (6) are periodic or quasi-periodic. In the lower panels $\gamma = 0.3$ and the non-Hamiltonian terms cause the fixed points in the centres to become repellers and all invariant tori to break up. On the long term solutions tend to attractors, i.e., orbits that closely follow the edges of the residual circulation cells. Solutions converge to different attractors, depending on their initial conditions and in some cases tracer orbits go from one circulation cell to another (see the blue and green curves in panel c). For the distribution of a tracer S this implies that at fixed locations (x,y) in the interior of each cell, in the course of time values of S are replaced by values of S that originate from locations that are closer to the center point of the cell). Furthermore, near the edges of each cell strong variations in S will occur (unless the initial distribution of S is spatially uniform).

The effect of adding non-Hamiltonian terms is also evident from the approximate analytical tidal map (38). As was shown in Section 3, adding these terms do not affect the fixed points of the Hamiltonian system, but they do affect their stability properties. When computing the eigenvalues of the tangent map, it follows that the fixed points that are elliptical for $\gamma = 0$ become unstable spiral points when $\gamma > 0$.

The reason that stable periodic orbits of the Hamiltonian system become unstable for $\gamma > 0$, can be deduced from analyzing the evolution of small elements $\delta V = \delta x \delta y$ in phase space along such periodic orbits. The equation for δV for our system (2b) reads

$$\frac{1}{\delta V}\dot{\delta V} = \frac{\partial \dot{x}}{\partial x} + \frac{\partial \dot{y}}{\partial y} \equiv D. \tag{41}$$

This result shows that if the averaged value of D, calculated along a periodic orbit, is positive, δV will grow in time and so, the orbit will be unstable.

In the present model D can be straightforwardly calculated. Moreover, it has a clear physical interpretation: since $\dot{x} = u$ and $\dot{y} = v$, D is the divergence of the Eulerian velocity field and it is determined by the continuity equation for depth-averaged tidal motion over a

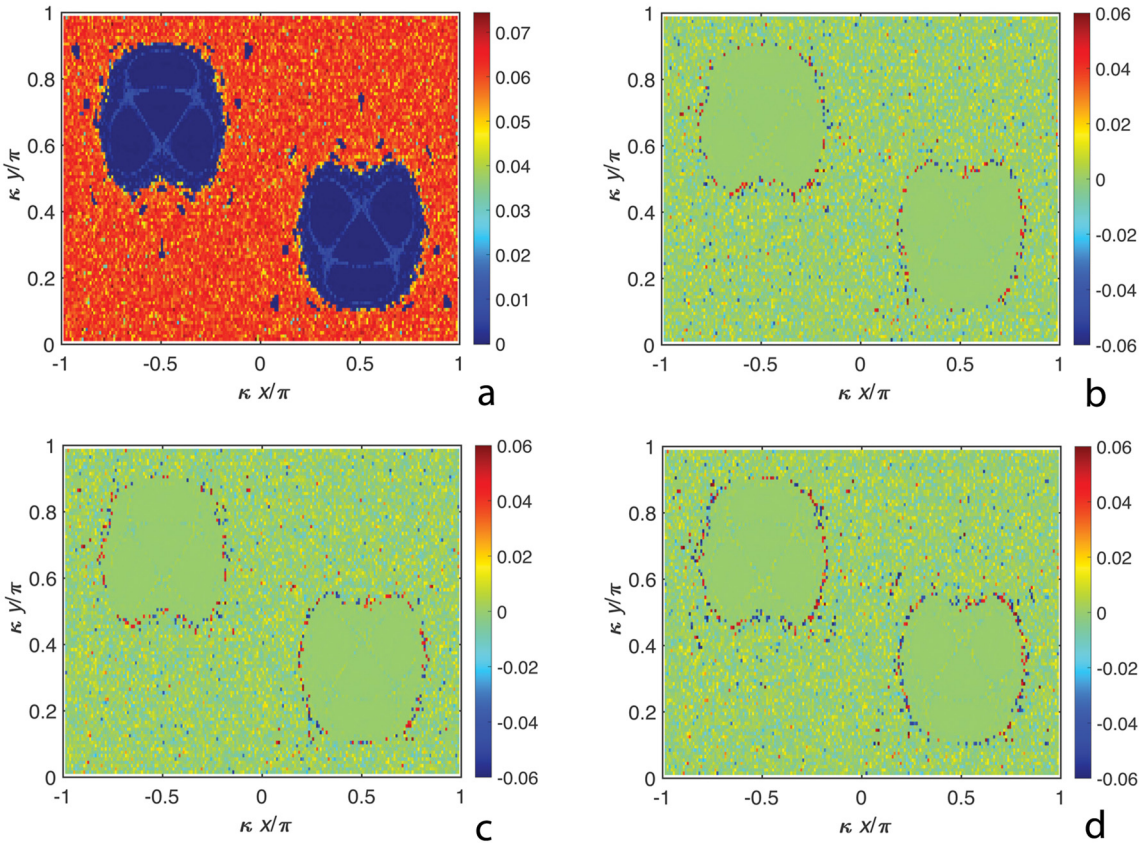

Fig. 6. As Fig. 5, but for $\kappa = \pi$, $\nu = 0.3$.

small-amplitude bottom topography (see [14] and Eq. (A1a) of SI-Appendix A):

$$D = -\cos(t)\frac{\partial h}{\partial x}, \tag{42}$$

with h denoting the variations in depth, given in Eqs. (5a) (5b) and shown in Fig. 1.

The averaged value of D can be calculated if the periodic orbit is known, which corresponds to a fixed point of the tidal map. Fig. 10 shows periodic orbits of system (6) for $\kappa = \pi/2$ and $\kappa = \pi$; the other parameters are $\nu = 0.3$ and $\gamma = 0.3$. The parts of the orbits where D is positive are colored red, while the blue parts indicate negative D. The sense of rotation of the orbits is anticlockwise. Clearly, along most part of the orbits D is positive, i.e. during flood ($\cos(t) > 0$) the parcel following this orbit is mostly in an area where $\partial h/\partial x \equiv h_x$ is negative, whereas during ebb ($\cos(t) < 0$) the parcel experiences mostly positive h_x. Near the turn of the tide, i.e., in the areas where the largest and smallest x-values are attained, values of D are variable, but also weak, because here both $\cos(t)$ are h_x are small (the latter is because $y \simeq \frac{1}{2}\pi/\kappa$). Thus,

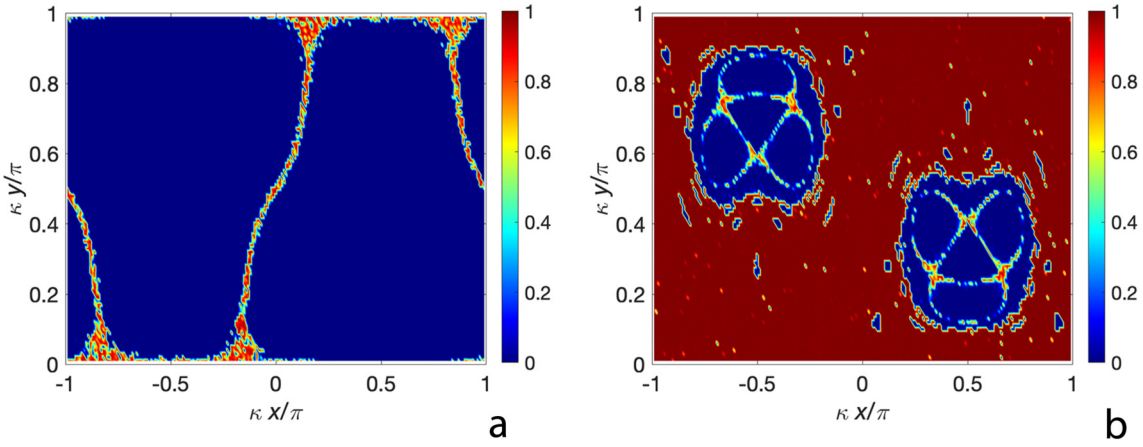

Fig. 7. Color plots of K-coefficient of the zero-one test for chaos, symplectic method, $\nu = 0.3$ and $\kappa = \pi/2$ (left) and $\kappa = \pi$ (right). (For interpretation of the references to color in this figure legend, the reader is referred to the web version of this article.)

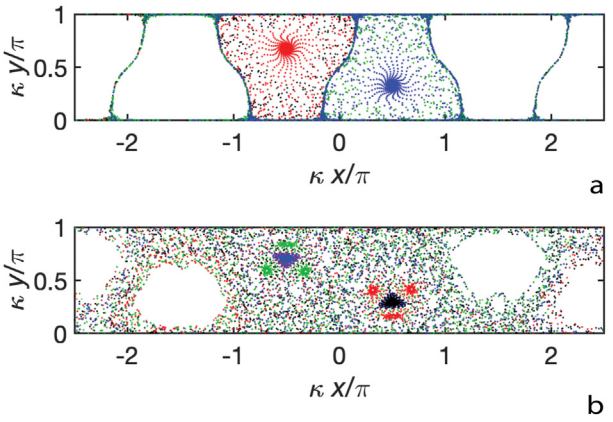

Fig. 8. As Fig. 4, but an additional non-Hamiltonian term is included in the system that originates from the velocity potential ϕ. Magnitude of this term is $\gamma = 0.01$.

the largest contributions to the averaged value of D occur when the tidal current is strong and these contributions are positive.

5. Discussion

To quantify the behavior of the model of tracer motion, which has no exact solutions, numerical methods were employed to simulate tracer orbits. As always, the challenge is to choose a suitable scheme. Here, three of them were considered: the built-in ode45 scheme of Matlab, RK4 and a new second-order scheme that conserves the symplectic structure of the Hamiltonian part of the system. The accuracy of each scheme could not be objectively determined using our dynamical system (6), as it has no exact solutions or constants of motion that can be used to assess the performance of the schemes. We therefore decided to apply the schemes to a test system that bears similarity to our system (it has a time-harmonic Hamiltonian and complex solutions), but its analytical solutions are known (see SI-Appendix C). The test system was configured such that its solutions were bounded and quasi-periodic.

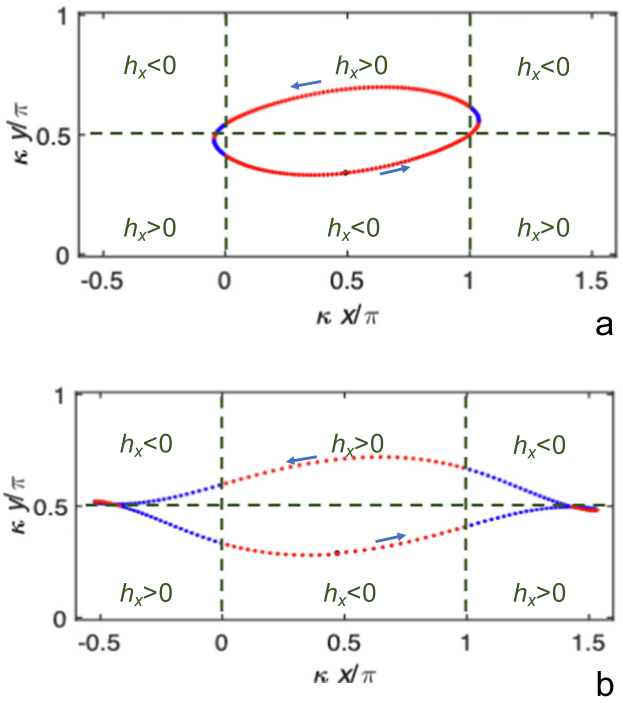

Fig. 10. Periodic orbits for $\kappa = \pi/2$ (panel a) and $\kappa = \pi$ (panel b), the values of the other parameters are $\nu = 0.3$ and $\gamma = 0.3$. The thick markers indicate the initial time $t = 0$ and arrows point the direction of increasing values of t. The orbit is colored red when the local value of flow divergence D is positive, whilst a blue color is used when D is negative. The variable $h_x = \partial h/\partial x$, with h the depth perturbation as is given in Eq. (5) and Fig. 1. (For interpretation of the references to color in this figure legend, the reader is referred to the web version of this article.)

The condition imposed for accuracy of each numerical scheme was that its relative error was slightly less than 0.01 after 1000 forcing periods. When subsequently being applied to our system 6, it appeared that, of the three schemes, the new scheme performs best, because it

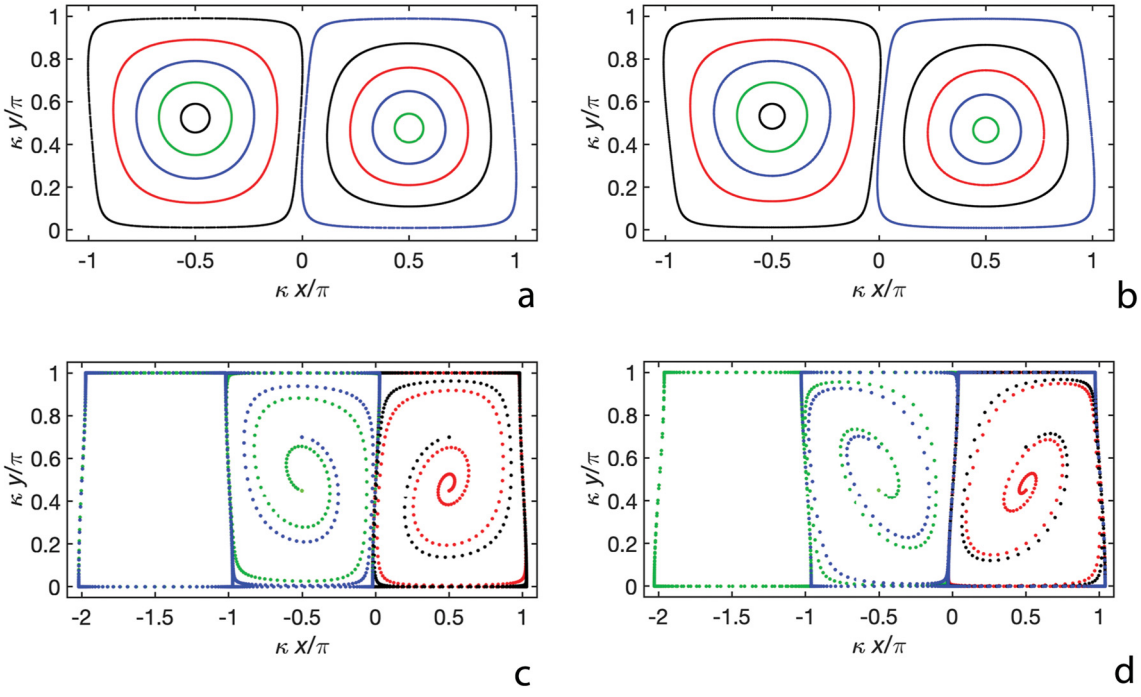

Fig. 9. a: Tidal map for $\nu = 0.04$, $\kappa = \pi/2$ and $\gamma = 0.0$ b) As a., but for $\kappa = \pi$ c. As a, but including the non-Hamiltonian velocity field, $\gamma = 0.3$. d. As c., but for $\kappa = \pi$.

conserves the symplectic structure of the Hamiltonian terms that occur in our model and moreover, it is a factor five faster than ode45 and RK4. The new scheme is of second order and could be extended to be of higher order (examples of higher order symplectic schemes are mentioned in [20]). However, it would be more difficult to design such schemes such that they can also deal with additional potential terms.

Note that the possibility to use a symplectic scheme relies on the condition that splitting of the stream function and velocity potential of the underlying velocity field can be achieved, so that each subsystem can be integrated in a simpler way than the original system. For our particular model this leads to Eq. (10). For most dynamical systems, splitting is indeed possible (see e.g. [16,21]). In the context of our problem, splitting would still be possible when additional time harmonics in the stream function and velocity potential would be included (only a few of the full set given in Eq. (3) are used), and also when the bottom topography in Eq. (4) would have additional spatial Fourier modes. While our scheme works well when using the idealized 2D hydrodynamic model of SI-Appendix A, it cannot be used to integrate particle orbits using gridded velocity data, as obtained from e.g. a sophisticated numerical hydrodynamic model, since no useful splitting of the velocity field determined by these data can be made. Thus, in these cases, Runge-Kutta schemes, as for example used in [8,9] and [22], are obvious choices.

To quantify the characteristics of orbits, we have calculated both the largest Lyapunov exponent and the K-coefficient of the zero-one test for chaos for various model settings and for a range of different initial conditions. The advantage of the largest Lyapunov exponent is that it has a clear meaning: it gives the mean growth rate of small perturbations that evolve on the principal orbit. In some cases however, their values are positive, but small. That raises the question whether they characterize orbits that are weakly chaotic, or whether the outcome is an artefact of the numerical method. According to their definition, Lyapunov exponents involve an integration over an infinitely long time. In our code, the value of the largest Lyapunov exponent λ is determined as follows. First $\lambda(T)$ is calculated for a time interval of at least 2000 tidal periods. When integration is continued over 1000 more tidal periods and changes in the value of the exponent are smaller than a certain tolerance (here $1 \cdot 10^{-4}$, then $\lambda = \lambda(T)$, otherwise T is increased. However, this method does not guarantee that for even larger value of T the criterion is not met. It is therefore very useful to calculate the K-coefficient of the zero-one test for chaos as well: any orbit that has a K-value that is close to 1 will be chaotic.

A remarkable feature is the occurrence of 'spikes' in the plots that show the changes in values of the largest Lyapunov exponent when e.g. a different time step or numerical scheme is used (see panels b–d in Figs. 5 and 6. A likely cause for their appearance is that for that parameter setting the system is fully Hamiltonian and its tidal map contains hyperbolic fixed points. Especially in the areas near the stable and unstable manifolds of these points, chaotic and regular orbits occur that can be at very close distance. In other words, when choosing a certain initial condition in that area, the joint occurrence of round-off errors and truncation errors might cause the simulated orbit to be chaotic or regular. This sensitivity does not decrease when for example choosing smaller time steps: the spikes will still occur.

It is important to stress that the velocity field that causes the advection of particles results from a model [14] that considers depth-averaged fluid motion over a bumpy bed. The result is a two-dimensional velocity field that is divergent and thus the equations describing tracer motion do not constitute a Hamilton system. This fact was ignored in previous studies on tracer motion in tidal seas ([6] and references herein), who only considered the part of the velocity field that is governed by the residual stream function. Our findings show that the divergent part of the velocity field, no matter how small, has a profound impact on tracer motion. It appears that periodic orbits, which are Lyapunov stable for $\gamma = 0$, become unstable for $\gamma > 0$. Moreover, in the latter case orbits tend to attractors in the tidal map, which (for the parameter values that we explored) are either limit cycles or strange attractors.

The hydrodynamic model that is used in this study is highly idealized. In natural tidal systems, tracers are subject to three-dimensional (3D) motion, they experience effects of Coriolis, wind, and they will be subject to Stokes drift resulting from both sea waves and phase differences in the tidal wave, etc. These aspects are accounted for in 3D numerical models (e.g. [22,23]). In our model a depth-averaged Stokes drift does occur (see Section 4.2), but its source is not the phase difference in progressive waves, but rather the joint action of a spatially uniform tidal current and Eulerian residual currents that are induced by tide-topography interaction.

Studies on tracer motion are important to gain more understanding on e.g. the fate of microplastic, transport of nutrients and salt, etc. In this context, it is important to discuss our findings in the context of the work of [23], who concluded that tides are not important for the net transport of plastics in the oceans. Indeed, in their model the role of tides is marginal, but the resolution of their model is such that it cannot account for tide-topography interactions at the scale of the tidal excursion, which is of the order of 10 km. Thus, net advection of floating microplastics by tides occurs at the subgrid scale of their model and needs to be parametrized. This could be done by using a model, like the one analyzed in this study, in which the model parameters (topographic wavenumber, bottom friction, amplitudes and phases of tidal constituents) are estimated from local bathymetric data and tidal data.

6. Conclusions

A model for tracer motion in shallow seas with a bumpy bed was studied. Trajectories of tracers were simulated for different velocity fields and model parameters, using different numerical schemes. The conclusions are as follows.

1. Three numerical schemes were tested: the built-in ode45 scheme of Matlab, a fourth order Runge-Kutta scheme and a new scheme. The latter is an extension of an existing symplectic scheme to systems that also contain non-symplectic terms. It was found that the latter performs best, because of its conservation properties and its short computation times.
2. Early simplified models considered advection of tracers by a velocity field that is fully described by a stream function ψ. Consequently, the equations governing tracer motion constitute a Hamilton system, with ψ being the Hamiltonian. However, depth-averaged velocity fields in tidal seas are divergent, resulting in additional components described by a velocity potential ϕ. When the latter is accounted for, no matter how small its magnitude, it causes major changes in the behavior of the tracers: net displacements will be towards attractors.
3. To characterize the behavior of tracer orbits, it is recommended to calculate both the largest Lyapunov exponent and the K-coefficient for chaos. The latter are particularly helpful when Lyapunov exponents are positive, but small.
4. Analysis of approximate analytical solutions and the related tidal map, obtained by the method of orbit expansion, turned out to be a helpful tool to interpret the behavior of the model.

CRediT authorship contribution statement

H.E. de Swart: conceptualization, methodology, simulations, writing - original draft preparation.
S.T. van der Wal: simulations, writing, reviewing.
J.E. Frank: numerics, reviewing.
G.P. Schramkowski: methodology, reviewing.

Declaration of competing interest

The authors declare that they have no known competing financial interests or personal relationships that could have appeared to influence the work reported in this paper.

Acknowledgements

This research did not receive any specific grant from funding agencies in the public, commercial, or not-for-profit sectors.

Appendix A. Supplementary data

Supplementary data to this article can be found online at https://doi.org/10.1016/j.chaos.2022.112318.

References

[1] Aref H. Stirring by chaotic advection. J Fluid Mech. 1984;143:1–21. https://doi.org/10.1017/s0022112084001233.
[2] Ottino JM. Mixing, chaotic advection, and turbulence. Annu Rev Fluid Mech. 1990; 22:207–53. https://doi.org/10.1146/annurev.fl.22.010190.001231.
[3] Tabor M. Chaos and integrability in nonlinear dynamics: an introduction. New York: John Wiley and Sons; 1989.
[4] Pasmanter R. Dynamical systems, deterministic chaos and dispersion in shallow tidal flow. In: Dronkers J, van Leussen W, editors. Physical processes in estuaries. Springer Verlag; 1988. p. 42–53.
[5] Ridderinkhof H, Zimmerman JTF. Chaotic stirring in a tidal system. Science. 1992; 258:1107–11. https://doi.org/10.1126/science.258.5085.1107.
[6] Beerens SP, Ridderinkhof H, Zimmerman JTF. An analytical study of chaotic stirring in tidal areas. Chaos Solitons Fractals. 1994;4:1011–29.
[7] Zimmerman JTF. Topographic generation of residual circulation by oscillatory (tidal) currents. Geophys Astrophys Fluid Dyn. 1978;11:35–47.
[8] Orre S, Gjevik B, LaCasce JH. Characterizing chaotic dispersion in a coastal tidal model. Cont Shelf Res. 2006;26:1360–74. https://doi.org/10.1016/j.csr.2005.11.015.
[9] Xu D, Xue H. A numerical study of horizontal dispersion in a macro tidal basin. Ocean Dyn. 2011;61:623–37. https://doi.org/10.1007/s10236-010-580 0371-6.
[10] Shimada I, Nagashima T. A numerical approach to ergodic problem of dissipative dynamical systems. Prog Theor Phys. 1979;61:1605–16.
[11] Benettin G, Galgani L, Giorgilli A, Strelcyn J-M. Lyapunov characteristic exponents for smooth dynamical systems and for hamiltonian systems; a method for computing all of them. Part 1: theory. Meccanica. 1980;15:9–20.
[12] Gottwald GA, Melbourne I. A new test for chaos in deterministic systems. Proc R Soc Lond A. 2004;2042:603–11.
[13] Gottwald GA, Melbourne I. The 0-1 test for chaos: a review. In: Skokos C, Gottwald GA, Laskar J, editors. Chaos detection and predictability. Berlin Heidelberg: Springer Verlag; 2016. p. 221–47. https://doi.org/10.1007/978-3-662-48410-4_7.
[14] Zimmerman JTF. Vorticity transfer by tidal currents over an irregular topography. J Mar Syst. 1980;38:601–30.
[15] Press WH, Teulkolsky SA, Vetterling WT, Flannery BP. Numerical recipes: the art of scientific computing. Cambridge University Press; 2007.
[16] McLachlan RI, Quispel GRW. Splitting methods. Acta Numer. 2002;11:341–434. https://doi.org/10.1017/S0962492902000053.
[17] Hairer E, Lubich C, Wanner G. Geometric numerical integration illustrated by the Störmer-Verlet method. Acta Numer. 2003;12:399–450. https://doi.org/10.1017/S0962492902000144.
[18] Abramowitz M, Stegun IA. Handbook of mathematical functions. New York: Dover Publications; 1965.
[19] Longuet-Higgins MS. On the transport of mass by time-varying ocean currents. Deep-Sea Res. 1969;16:431–47.
[20] Cartwright JHE, Piro O. The dynamics of Runge-Kutta methods, 605. Int J Bifurcation Chaos. 1992;2:427–49.
[21] Hairer E, Hochbruck M, Iserles A, Lubich C. Geometric numerical integration. Oberwolfach Rep. 2006;3(1):805–82.
[22] Stanev E, Badewien TH, Freund H, Grayek S, Hahner F, Meyerjürgens J, Ricker M, Schöneich-Argent RI, Wolff J-O, Zielinski O. Extreme westward surface drift in the North Sea: public reports of stranded drifters and lagrangian tracking. Cont Shelf Res. 2019;177:24–32. https://doi.org/10.1029/2019JC01558.
[23] M. Sterl P. Delandmeter E. van Sebille , Influence of barotropic tidal currents on transport and accumulation of floating microplastics in the global open ocean, J Geophys Res Oceans 125, e2019JC015583. doi:10.1029/2019JC01558.